Department of Physics and Astronomy
University of Heidelberg

Bachelor Thesis in Physics
submitted by

Michael Rosner

born in Marktredwitz (Germany)

2017

The CANREB Electron Beam Ion Source:
Laser Ion Source and Beam Line Assembly

This Bachelor Thesis has been carried out by Michael Rosner at the
Max-Planck-Institut für Kernphysik (MPIK) in Heidelberg
under the supervision of
Priv.-Doz. Dr. José Ramón Crespo López-Urrutia

Abstract

A Laser Ion Source (LIONS) was set up with a beam line including an image-charge detector in order to test the efficiency of a charge breeding unit, in this case an Electron Beam Ion Trap (EBIT). The parameters of LIONS and the beam line were optimized in order to maximize the number of singly charged ions. Ion quantities of up to $1.14(17) \times 10^9$ singly charged ions were achieved during the tests. The image-charge detector was designed to allow bidirectional measurements of the charge of the same ion bunch during injection in and extraction out of the charge breeder respectively. It therefore enables a charge distribution analysis before and after charge breeding.

Eine Laser-Ionenquelle (LIONS) mit dazugehöriger Strahllinie, die einen Spiegelladungsdetektor beinhaltet, wurde aufgbaut und in Betrieb genommen, um die Effizienz eines Ladungsbrüters, in diesem Fall einer Elektronenstrahl-Ionenfalle, zu messen. Die Betriebsparameter der LIONS und der Strahllinie wurden auf die Ausbeute einfach geladener Ionen maximiert. In den Tests wurden bis zu $1.14(17) \times 10^9$ einfach geladene Ionen nachgewiesen. Der Spiegelladungsdetektor wurde so konstruiert, dass er eine bidirektionale Messung der selben Ionengruppe sowohl bei der Injektion in als auch bei der Extraktion aus dem Ladungsbrüter ermöglicht. Er erlaubt also eine Analyse der Ladungszustandsverteilung vor und nach dem Brüten.

Contents

Chapter 1

Introduction

"The elementary particles are certainly not eternal and indestructible units of matter, they can actually be transformed into each other. As a matter of fact, if two such particles, moving through space with a very high kinetic energy, collide, then many new elementary particles may be created from the available energy and the old particles may have disappeared in the collision. Such events have been frequently observed and offer the best proof that all particles are made of the same substance: energy."
— Werner Heisenberg [1]

Probably one of the oldest school of ancient philosophy is the *philosophia naturalis*, the study of nature, which evolved to what we nowadays call natural science [2]. Part of that school was to find out what the world consists of. Back in the 5th century B.C. the Greek philosopher Democritus constituted that there is an infinite number of indestructible, undividable and indistinguishable entities in free space making up everything else through collision and entanglement [3]. They were named $\alpha\tau o\mu o\nu\sigma$ - atoms. While we still use the term atom today, it was discovered that the properties described by Democritus do not hold up. At the beginning of the 19th century A.D. John Dalton constituted all matter consits of elements - atoms, that can not be split anymore through chemical analysis - and, what we today call a molecule, different atoms "retained in physical contact by a strong affinity" [4]. Different theories how the atom looks like evolved, leading from J. J. Thomson's plum pudding model to the Rutherford model and the Bohr model. Here, the atom is divided in a nucleus and and some kind of shell, which led to the distinction between atomic and nuclear physics [5]. Atomic physics then refined the atomic models resulting in a quantum mechanical description, with W. Heisenberg allegedly saying, one should not even try to imagine how an atom looks like [6]. On the other hand, in nuclear physics,

Rutherford showed that the nucleus can be changed, making oxygen out of nitrogen by shooting alpha particles at it [7]. Further experiments led to the discovery that the nucleus consists of neutrons and protons. A nucleus combined with electrons is an atom, which is consistent with the quantum mechanical description [7]. Subsequently Hahn, Straßmann and Meitner were able to conduct the first nuclear fission in 1938 [7].

In the middle of the 20th century different institutions tried to create new elements which don't occur naturally. The successful ones are the Lawrence Berkeley National Laboratory in the US, Flerov Laboratory of Nuclear Reactions, part of the Joint Institute for Nuclear Research, in Russia and the GSI Helmholtz Centre for Heavy Ion Research in Germany [8]. Others aim to produce stronger beams of rare isotopes of known elements, like the Grand Accélérateur National d'Ions Lourds in France, the CERN in Switzerland, the Oak Ridge National Laboratory in the United States or the Advanced Rare Isotope Laboratory (ARIEL) currently under construction at the TRIUMF institute in Canada [9].

To fulfill its purpose, ARIEL consists of a linear electron accelerator with up 50 MeV, 10 mA as well as of a cyclotron to produce an proton beam with up to 100 μA, two Isotope Separation On-Line target stations and a connection to the ISAC-I and ISAC-II accelerator complexes with additional mass separators [9]. On ARIEL, the new accelerator path, CANadian Rare-isotope facility with Electron-Beam ion source (CANREB), it was decided to use an electron beam ion source (EBIS) as a charge breeder before acceleration in order to use lower acceleration voltages [10]. Advantages against conventional charge breeding devices like an electron-cyclotron-resonance ion source (ECRIS) are less contamination, higher efficiency and higher charge states [10]. The objective here is to reach a mass-to-charge ratio of $5\,\mathrm{u}\,e^{-1}$ to $7\,\mathrm{u}\,e^{-1}$. To test the functionality of the EBIS it was decided to use a Laser Ion Source (LIONS). Here the setup of the LIONS and of the beam line for the tests is discussed and the LIONS is characterized with a couple of measurements. It is further planned to connect the LIONS to the EBIS with an image-charge detector and an additional two-sided faraday cup to investigate the properties of injected and extracted ions. This would allow a direct efficiency measurement of the EBIS, as it allows the non-destructive detection of a minimum of 3×10^3 ions on-line [11].

Chapter 2

Theoretical Basics

2.1 Laser

To create a plasma the LIONS uses a laser. As primary source for the theory of laser [12] was used. The acronym laser stands for Light Amplification by Stimulated Emission of Radiation. The emission occurs in the so called gain medium which is pumped with energy. Possible ways for pumping include light from flashbulbs or other lasers as well as electrical effects in semiconductors. In the medium we have an ensemble of N systems with different initial energy statesF $|i\rangle$, therefore:

$$N = \sum_i N_i \tag{2.1}$$

The fundamental processes between the states, $|i\rangle$ and $|j\rangle$, w.l.o.g. $E_i < E_j$, are:

- The *absorption* of a photon of the energy $h\nu = E_j - E_i$ to induce a transition $|i\rangle \to |j\rangle$. With a energy density $u(\nu)$ in the gain medium the transition rate

$$\left(\frac{\mathrm{d}N_j}{\mathrm{d}t}\right)_{\mathrm{abs}} = -\left(\frac{\mathrm{d}N_i}{\mathrm{d}t}\right)_{\mathrm{abs}} = B_{ij}u(\nu)N_i \tag{2.2}$$

  is quantified by the Einstein coefficient B_{ij} [12].

- The *spontaneous emission* of a photon with the energy $h\nu = E_j - E_i$ with random phase in a random direction. The transition $|j\rangle \to |i\rangle$ hereby happens at a rate

$$\left(\frac{\mathrm{d}N_j}{\mathrm{d}t}\right)_{\mathrm{spon}} = -\left(\frac{\mathrm{d}N_i}{\mathrm{d}t}\right)_{\mathrm{spon}} = -A_{ji}u(\nu)N_i \tag{2.3}$$

which only depends on the number of systems in state $|j\rangle$ and is quantified by the Einstein coefficient A_{ji} [12].

- The *stimulated emission* of a photon with energy $h\nu = E_j - E_i$ induced by another photon of the same energy. Both photons are identical in all their properties, e.g. phase, direction, wavelength and polarization. The transition $|j\rangle \to |i\rangle$ is induced with a rate

$$\left(\frac{\mathrm{d}N_j}{\mathrm{d}t}\right)_{\mathrm{stim}} = -\left(\frac{\mathrm{d}N_i}{\mathrm{d}t}\right)_{\mathrm{stim}} = -B_{ji}u(\nu)N_i \qquad (2.4)$$

  at the energy density $u(\nu)$ and is quantified by the Einstein coefficient B_{ji} [12].

Since, as it can be shown, the Einstein coefficients are symmetrical,

$$B_{ji} = B_{ij} \qquad (2.5)$$

more than two energy levels are needed to get a population inversion ($N_j > N_i$) needed for a laser to have net stimulated emission [12]. Without a population inversion the absorbed light would exceed the emitted. The easiest way to achieve population inversion is a third energy level above both others, $|k\rangle, E_k > E_j > E_i$, with a high spontaneous transition rate for $|k\rangle \to |j\rangle$. To get a population inversion here energy is added in a fashion that it powers the transition $|i\rangle \to |k\rangle$, followed by $|k\rangle \to |j\rangle$ [12]. The rate of the transition $|i\rangle \to |k\rangle \to |j\rangle$ is nearly the same as $|i\rangle \to |k\rangle$, with ideally $N_k \approx 0$. Obviously at least $50\,\%$ of N needs to be pumped into $|j\rangle$ to get a population inversion, which requires a pump rate of at least $A_{ji}N_j > A_{ji}0.5N$. This is possible but ineffiecent. A more efficient way is to use four energy levels $E_k > E_j > E_i > E_h$, with fast spontaneous transitions $|k\rangle \to |j\rangle$ and $|i\rangle \to |h\rangle$ leading to $N_k \approx 0$ and $N_i \approx 0$. Hence any population $N_j > 0$ is an inversion [12].

In either of these configurations a stimulated emission of the transition $|j\rangle \to |i\rangle$ is desired. According to Equation 2.4 that depends on the population state, which we discussed above, and the energy density of the appropriate wavelength. Since the emitted light (both, through spontaneous and stimulated emission) has the appropriate energy, the light only needs to be trapped inside a so called optical resonator. The resonator is characterized with the quality factor

$$Q(\omega) = \omega \frac{\text{stored energy}}{\text{power loss}} \qquad (2.6)$$

describing what fraction of energy leaves the cavity [12]. For a continuous wave laser there is always a power "loss": the beam leaving the cavity. Here, an equilibrium is built up between energy leaving the cavity and energy being pumped in, leading to a constant beam power.

Another possibility is to use a Q-switch to get a pulsed beam. Here the power loss at first is very high so nearly no energy is stored in the resonator. Therefore the stimulated emission is suppressed and the population inversion can increase further than for a continuous wave laser. Now Q is rapidly increased. Thus energy density ascends exponentially, decreasing the population inversion. The energy density falls rapidly. In that fashion, very short pulses with high energies are formed.

Because laser beams are formed through stimulated emission, they normally are highly coherent, precisely directed and have a small bandwidth of wavelengths. They often have a fixed polarization as well [12].

2.2 Plasma

Often called the fourth fundamental state of matter, the term plasma refers to matter with higher energies than gas so that it is at least partially ionized [13]. As it is the key ingredient for ion sources, its theory is explained here, mainly according to [13]. Ions and free electrons coexist in a plasma, which makes it electrically conducting. In nature that state occurs for example in stars, the ionosphere or in transient forms like lightning. In technology plasmas are used in various forms of application, like illumination, in semiconductor processing, fusion research, manufacturing and much more.

The main parameters to describe a plasma are the *plasma density*, the *degree of ionization* and *plasma temperature*. The plasma consists of ions, described by the ion density n_i, electrons, described by the electron density n_e and neutral particles described by their density n_n. The different positive ion charge states, $q_i = 1+, 2+, 3+, ...$, are possible, or in some conditions also negative ones, $q_i = 1-, ...$ However, the total charge neutrality is preserved. This leads to the condition

$$\sum q_i n_i = n_e. \tag{2.7}$$

The term *plasma density* then describes either the electron density or the ion density, which can be ambiguous for plasmas with ions with $q_i \neq 1+$. To have a clear or more extensive description of the plasma, one can specify the electron density n_e as well as the distribution of charge states. The *degree of ionization*, defined as the ratio of the density of ionized particles to the total density of ions and neutral particles,

$$\text{degree of ionization} = \frac{n_i}{n_i + n_n}, \tag{2.8}$$

is another parameter to classifiy a plasma. If the degree of ionization is 1, the plasma is called

fully ionized. The term *highly ionized* is used in different manners, on the one hand for plasmas with a degree of ionization of about 10% or more and on the other for plasmas with many ions with more than one electron removed. The latter one might be called "highly stripped" or "multiply ionized" instead [13]. The last typical parameter is the *plasma temperature* which traditionally is given in electron volts, with

$$1\,\text{eV} = 11\,600\,\text{K} \tag{2.9}$$

Important to note here is, that the plasma temperature is not necessarily equal for all parts of the plasma. It can be different for ions and for electrons or even different for one particle, since in a magnetic field there is an anisotropy leading to different temperatures parallel and orthogonal to the magnetic field. Furthermore, plasma temperature should not to be confused with the plasma drift energy, which can be of quite different magnitude.

2.2.1   Thermal Plasma

The term *thermal plasma* is used for plasmas in a thermal equilibrium, where the velocity distribution function $f(\vec{v})$, giving the number of particles n at a certain velocity, is normally distributed:

$$f(\vec{v}) = n \left(\frac{m}{2\pi T}\right)^{\frac{3}{2}} e^{-\frac{m\vec{v}^2}{2T}}. \tag{2.10}$$

Here T is the plasma temperature in energy units and m is the mass of the particle. An integration over all directions leads to the distribution of the absolute speed

$$f(v) = 4\pi v^2 n \left(\frac{m}{2\pi T}\right)^{\frac{3}{2}} e^{-\frac{m\vec{v}^2}{2T}} \tag{2.11}$$

and then to the energy distribution

$$f(E) = f(v)\frac{\mathrm{d}v}{\mathrm{d}E} = n\sqrt{\frac{4E}{\pi}}T^{-\frac{3}{2}}e^{-\frac{E}{T}}. \tag{2.12}$$

For the mean values follows

$$\bar{v} = \sqrt{\frac{8T}{\pi m}} \tag{2.13}$$

and

$$\bar{E} = \frac{3}{2}T. \tag{2.14}$$

While, as noted above, the plasma in total is neutral, it consists of positive and negative charged

particles that can move separately. Since, according to Equation 2.13, light particles, like electrons, are moving faster than heavy particles, like ions, the thermal movement leads to an electric force inside the plasma. This force drives the faster diffusing electrons back into the plasma and leads to an oscillation of the electrons around the ions with the *plasma frequency*

$$\omega_p = \sqrt{\frac{e^2 n_e}{\epsilon_0 m_e}} \tag{2.15}$$

where ϵ_0 denotes the permittivity of vacuum [13]. So the plasma is held together via electrical forces but is electrically neutral overall, an effect called quasi-neutrality. This quasi-neutrality also influences the dynamics inside the plasma, as the electrical force on a particle only comes from the other particles nearby and doesn't propagate through the whole plasma. Inside an outer electric field, the same effect occurs: In an outside layer of the plasma, the differently charged particles are redistributed in a fashion that compensates for the outer field and keeps the inside on a constant potential. The effect decreases exponentially over the distance and depends on the plasma temperature and electron density. The thickness of this outer region of the plasma, called *plasma sheath*, is characterized with the scale length called the *Debye length* [13]

$$\lambda_{\mathrm{D}}^2 = \frac{\epsilon_0 T_{\mathrm{e}}}{e^2 n_{\mathrm{e}}} \tag{2.16}$$

2.2.2 Laser Plasma

If a sufficiently strong laser is focused on the surface of a solid material, a plasma will form through thermal ionization, even if the photon energy is below the ionization energy. This happens due to the transmitted thermal energy which mainly depends on the laser intensity I as well as on the absorption coefficient α and the reflection coefficient R of the material [14].

$$I = \left| \vec{E} \times \vec{H} \right| = n_1 \epsilon_0 \vec{E}^2 \tag{2.17}$$

$$\alpha = -\frac{1}{I}\frac{\mathrm{d}I}{\mathrm{d}z} = \frac{4\pi n_2}{\lambda} \tag{2.18}$$

$$R = \left| \frac{n-1}{n+1} \right|^2 \tag{2.19}$$

Where $n = n_1 + in_2$ is the refractive index with its real component n_1 and its imaginary component n_2. This leads to a specific power of

$$J(z) = I(1 - R) \left(1 - \exp\left[-\int_0^z \alpha(r)\,\mathrm{d}r \right] \right) \tag{2.20}$$

at the depth z inside the material. Of course this holds only for weak pulses which do not change the structure of the material. For the high laser intensities needed to create a plasma, this obviously is not the case. On the contrary, the optical properties change quite a lot [15]. The main mechanism are:

- Increased temperature which changes the density and electric properties [14]

- Creation of free charge carriers which increase the absorption coefficient [14]

- Nonlinear effects on electron orbitals due to the intense electrical field of the laser beam. This leads to effects like self-focusing and multi-photon absorption [14].

In a time frame of about $100\,\mathrm{fs}$ the energy is distributed over the crystal structure [14]. For high intensities, this leads to melting and evaporation. When the laser frequency reaches the plasma frequency, the reflection and absorption coefficient change rapidly. As a result, the temperature increases even more and a plasma is created. The highly raised pressure leads to an acceleration of the plasma away from the target. The structure of the laser pulse therefore influences the plasma parameters at different locations in the plasma [14].

2.3   Beam Line

2.3.1   Creation and Accelaration of the Ions

The ions in the plasma have a main velocity component, in the direction of the electrical field, away from the target, and one perpendicular to it. That spreads the plasma in a certain solid angle. Therefore the plasma density decreases with the distance from the target to the power of -3 . This leads to a change of the Debye length over the distance. An increased potential U_{ex} inside the propagating plasma would form a plasma sheath in the range of that length at its border and lift the inside of the plasma on said potential. The resulting electrical potential can be seen schematically in Figure 2.1. This leads to a charge separation in the plasma sheath on all borders. The separated ions are then accelerated with its effective acceleration voltage $U_{\mathrm{acc}} < U_{\mathrm{ex}}$ since it is partially shielded by the rest of the plasma. This leads to a total ion energy
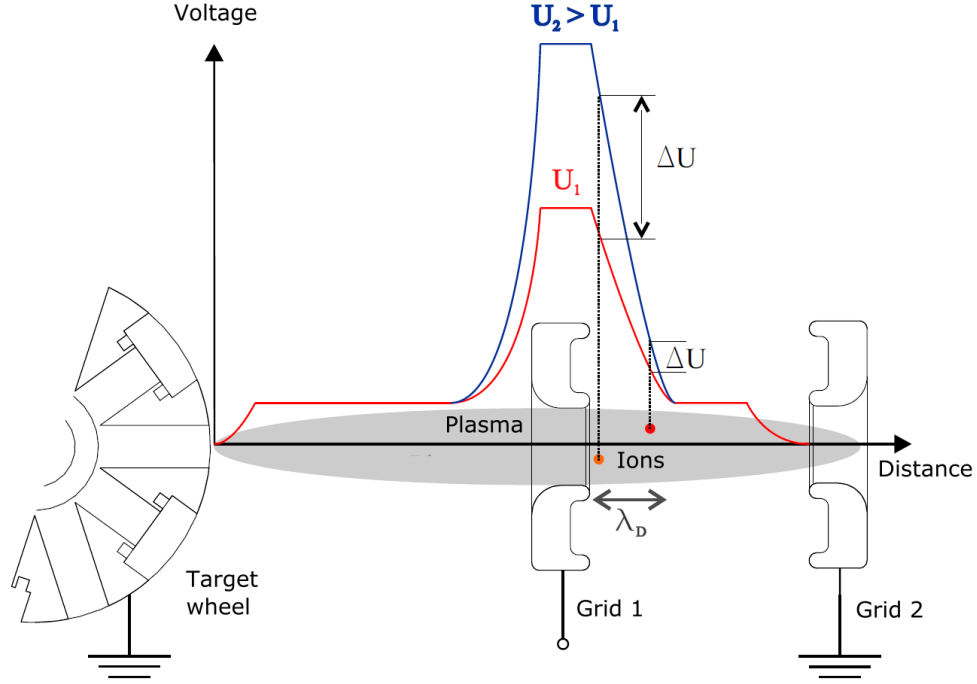
Figure 2.1: Schematic of the acceleration grids with resulting electrical potential inside the plasma with a plasma sheath of length λ_D for different applied voltages U_1 and U_2, adapted from [14].

of

$$E_{\mathrm{ion}} = E_0 + U_{\mathrm{acc}}q \tag{2.21}$$

consisting of the initial drift energy E_0 and the additional electrical energy $U_{\mathrm{acc}}q$. It is further assumed that $U_{\mathrm{acc}} \propto U_{\mathrm{ex}}$.

2.3.2   Ion Optics

An ion beam can be deflected using an electrostatic quadrupole potential of the form

$$V = K(x^2 + y^2) \tag{2.22}$$

where K is a constant of proportionality and x and y are the coordinates in the plane of the beam with the origin at the center of the quadrupole. The beam enters on one of the axes, e.g.

the x-axis, and should leave after a 90° bend, e.g. on the y-axis. The strength of the quadrupole, represented by K, should be chosen accordingly. It has been shown that there is in fact an infinite number of paths an ion can have in an electrical quadrupole field to perform a 90° bend, but only one of them leads to reasonable results [16]. That path of course crosses the hyperbolic equipotentials of the quadrupole field. Therefore it is clear that the velocity of the ions in direction of the ion path has to change, since its energy increases. It is a conservative field, so the approximations done for a Sikler lens in [17] hold here as well. Defining τ as local direction of the ion path, it follows for the acceleration in τ direction a_τ:

$$a_\tau = \frac{F_\tau}{m} = \frac{qE_\tau}{m} = \frac{q}{m}\left(-\frac{\mathrm{d}V}{\mathrm{d}\tau}\right). \tag{2.23}$$

For a constant field

$$\left(-\frac{\mathrm{d}V}{\mathrm{d}\tau}\right) \propto U_{\mathrm{qu}} \Rightarrow a_\tau \propto U_{\mathrm{qu}} \Rightarrow a_\tau \propto \frac{q}{m} \tag{2.24}$$

follows. This effect only influences the time of flight through the quadrupole and not afterwards, since the potential before and after the quadrupole is the same and therefore guarantee the same energy of the ions. The accelerations proportionality to q/m, that holds for all directions, also has the advantage, that particles with the same acceleration voltage take the same path through the quadrupole field.
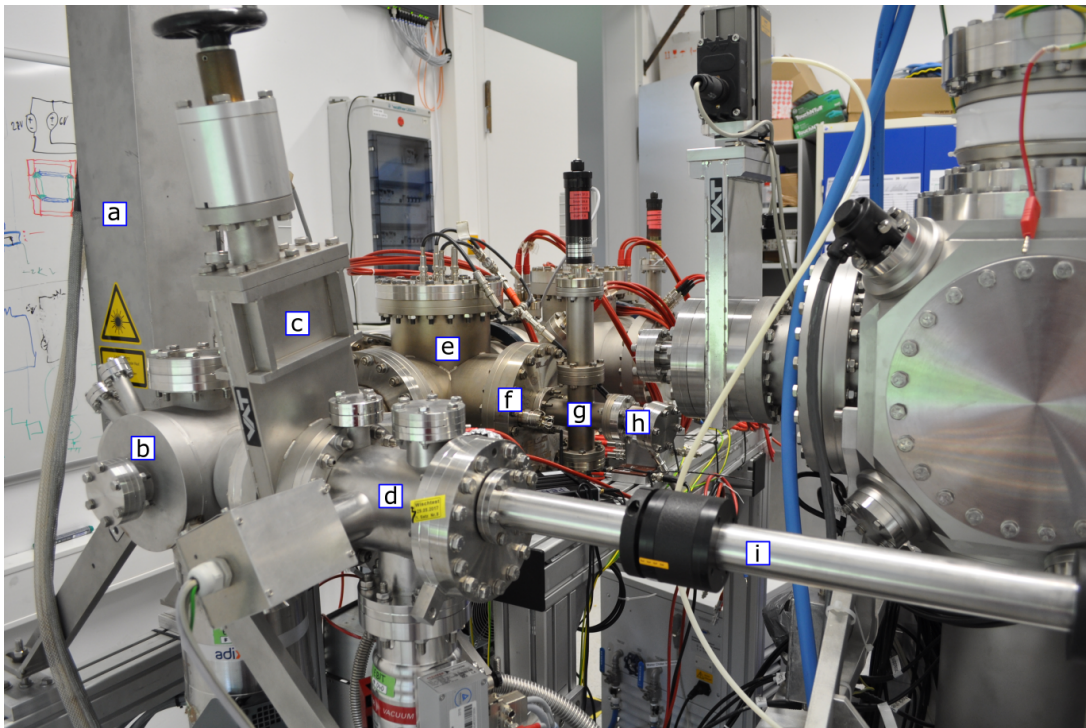
Chapter 3

Experimental Setup

Figure 3.1: Photography of the experimental setup. (a) laser and laser optics, (b) target position, (c) valve between ion source chamber and target exchange chamber, (d) chamber for target exchange without venting the whole ion source chamber, (i) manipulator to move the target wheel between ion source and target exchange chamber, (e) quadrupole bender, (f) quadrupole triplet 1, (g) Faraday cup 1, (h) connector of the LIONS to the EBIT.
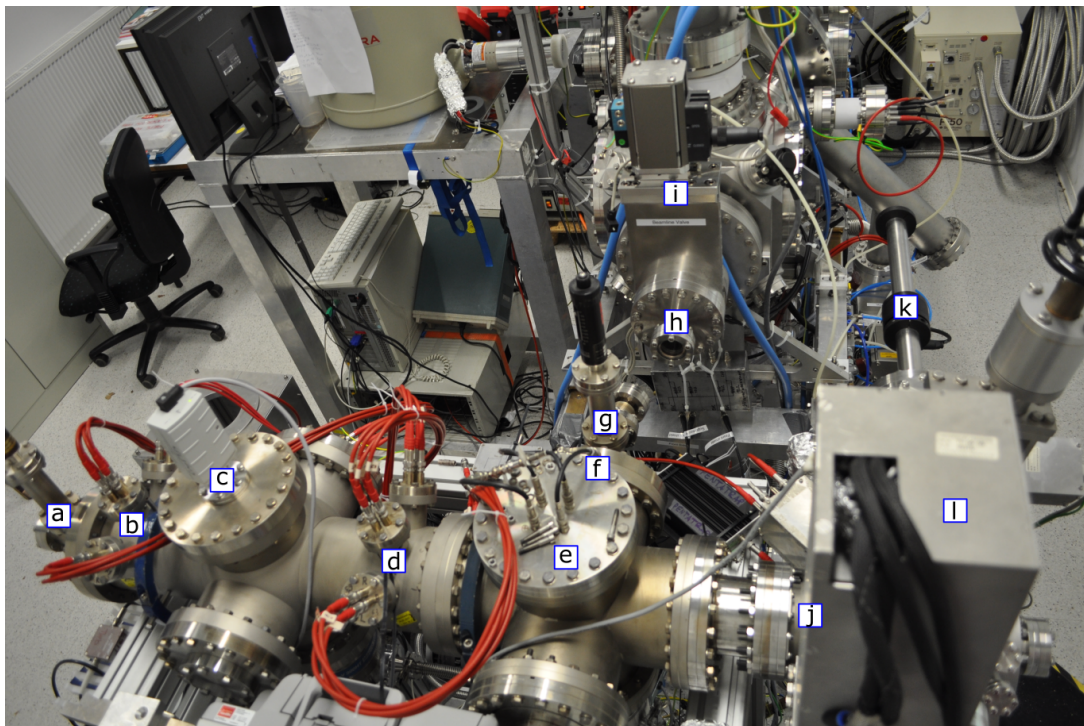
Figure 3.2: Photography of the experimental setup with the charge breeder in the background. (a) Faraday cup 2 (b) quadrupole triplet 3, (c) pressure gauge, (d) quadrupole triplet 2, (e) quadrupole bender, (f) quadrupole triplet 1, (g) Faraday cup 1, (h) connector of the EBIT to the LIONS, (i) EBIT, (j)Einzel lens and acceleration grids, (k) manipulator of the target wheel, (l) laser.

The experimental setup is divided into two main vacuum chambers. The first of them houses the laser ion source with the laser mounted outside the vacuum as well as the acceleration grids and an Einzel lens which was not used in this experiment. The second one consists of different ion optics and two Faraday cups. in this experiment, one cup and the quadrupole bender were used for the measurements. The whole setup can be seen in Figure 3.1 and 3.2.

3.1   Laser Ion Source

The Laser Ion Source (LIONS) is composed of two differentially pumped vacuum chambers, which allows for fast exchange of the targets, and of a laser setup with laser optics outside the vacuum [14]. The function principle was described in Chapter 2 and can be seen in Figure 3.3.
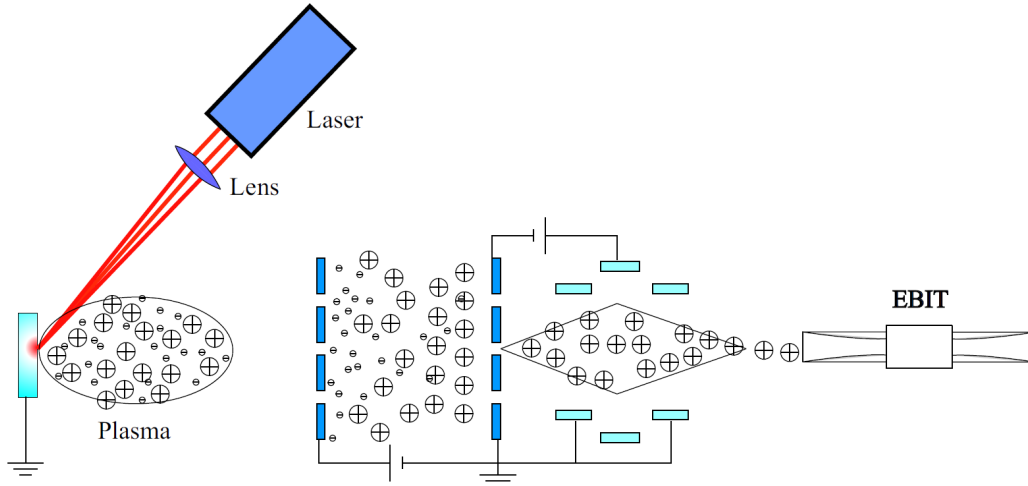
Figure 3.3: Principal of the ion creation in the LIONS: The laser hits the target and creates a plasma. The plasma reaches the extraction grid where an extraction voltage leads to charge separation and acceleration of the whereby created ions. Adapted from [14].

3.1.1 Laser

The laser used here is a Nd:YAG laser which is pumped with a flashbulb and emits light with pulse energies up to $50\,\text{mJ}$ at a pulse length of $8\,\text{ns}$ at a wavelength of $1064\,\text{nm}$. With a frequency doubling stage laser pulses with $30\,\text{mJ}$, $7\,\text{ns}$ and $532\,\text{nm}$ can be emitted. The maximum repetition rate is $20\,\text{Hz}$. The path of the laser through its optics can be seen in Figure 3.4. lens 1 widens the laser beam, so the power density isn't too strong on the following optical elements. lens 2 then collimates the beam and can be adjusted to focus the beam on the target. mirror 1 then reflects the beam through a window into the vacuum chamber where lens 3 focuses the beam and mirror 2 reflects it onto the target. Between mirror 2 and the target is a glass shield to prevent the plasma to hit the laser optics. The inclination angle on the target is roughly $23°$. The estimated focus radius through this setup at the maximum laser intensity is about $50\,\mu\text{m}$. The losses through ray optics are about $25\,\%$. This leads to a power density of $10^{11}\,\text{W}\,\text{cm}^{-2}$ well above the needed density of about $10^{8}\,\text{W}\,\text{cm}^{-2}$ for plasma creation [14].

3.1.2 Target

The target is mounted on a rotatable wheel with the possibility to mount up to five different targets. This has numerous advantages compared to a fixed target:

1. One can change the element from target to target in a matter of seconds, without the need of any tools or opening up a vacuum chamber, for better reproducibility of experimental conditions.

2. If a slot is left open, the wheel can be rotated so ions can go through the target wheel into an additional beam line behind it.

3. The target wheel can be moved slightly to change the laser position on the same target so that no serious damage on the target surface is generated.

The rotation of the wheel is divided in 200 steps, which allows for turns of $1.8°$, but smaller steps would allow to use even more of the target surface [14].

3.1.3 Acceleration Grids

The last part of the LIONS is the grid where the extraction voltage is applied. The setup can be seen in Figure 3.5. The voltage is applied to the first grid. If the voltage is applied continuously, this results in a charge separation even before the plasma reaches the grid, repelling the ions back to the target and not extracting them in the direction of the second grid. There are different ways around this, like putting the target on the extraction potential as well or applying the voltage in a pulse after the laser. The second method is used here, therefore the first grid is connected via a BEHLKE fast high-voltage switch [18] to a delay gate. The start signal delivered to the delay gate comes from the Q-Switch of the laser which occurs roughly $70\,\text{ns}$ before the laser pulse [14]. After a delay time t_d the delay gate sends a signal with the pulse length t_p to the high-voltage switch. After a time of $100\,\text{ns}$ it applies the extraction voltage U_ex on the first grid for the duration of t_p. This way the charge separation is induced after the plasma is past the first grid, accelerating it in direction of the second grid. Since that happens somewhere in the plasma sheath, there is an uncertainty in the exact location of the accelerated ions at the time of acceleration as well as in the acceleration voltage. Also mounted in the LIONS chamber is an Einzel lens between the grids and the beam line, which here was grounded and therefore simply acted as an aperture.
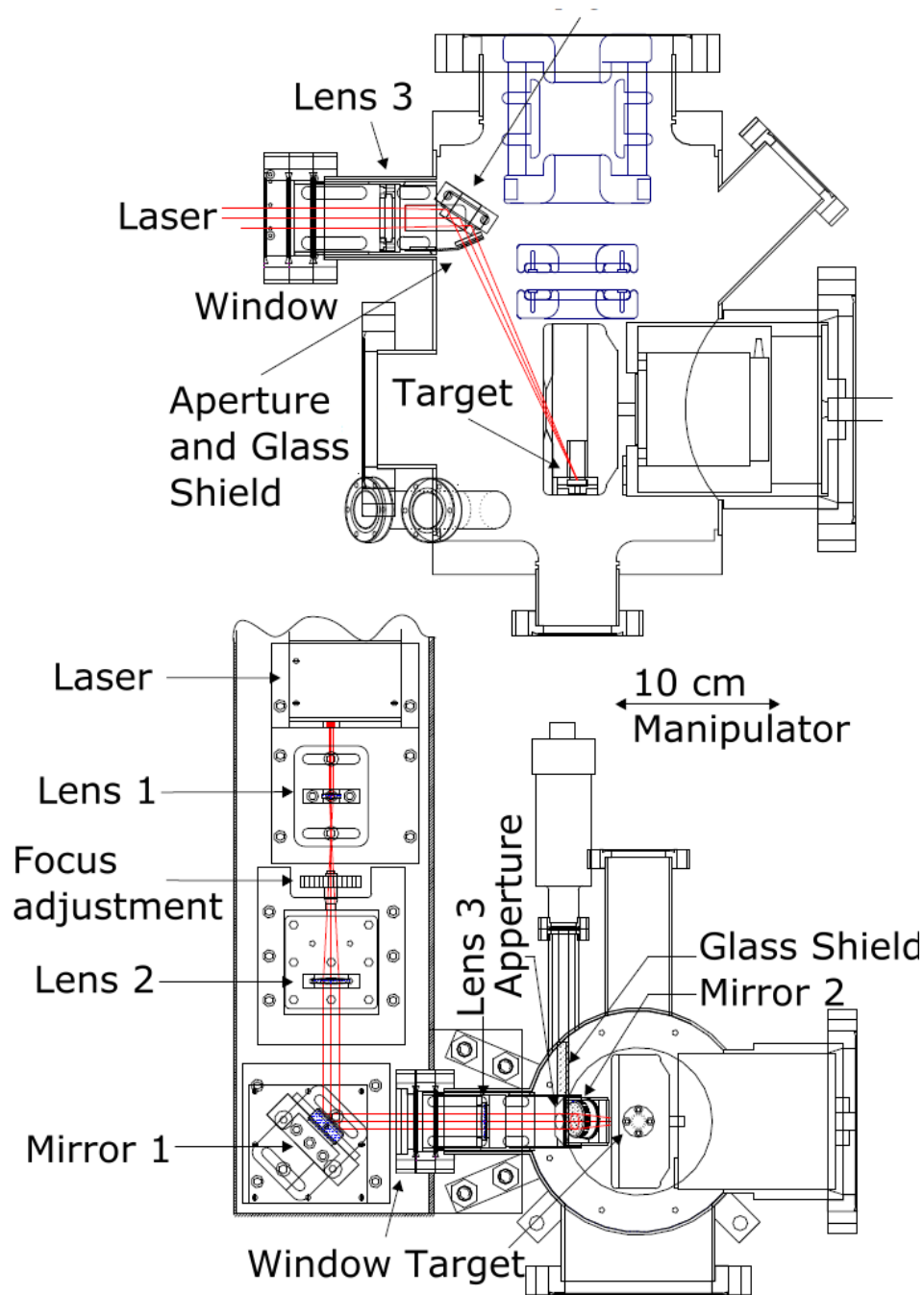
Figure 3.4: Sectional views through the laser optics. Upper: Horizontal cross-section. Lower: Vertical cross-section. The Laser is wiedened between lens 1 and lens 2. lens 2 can be moved vertically to allow adjustment of the focus. It enteres the vaccum chamber through the window after reflection by mirror 1. Lens 3 focuses the beam on the target which is reached after reflection by mirror 2. Between mirror 2 and the target is a glass shield to protect the optical parts. Adapted from [14].
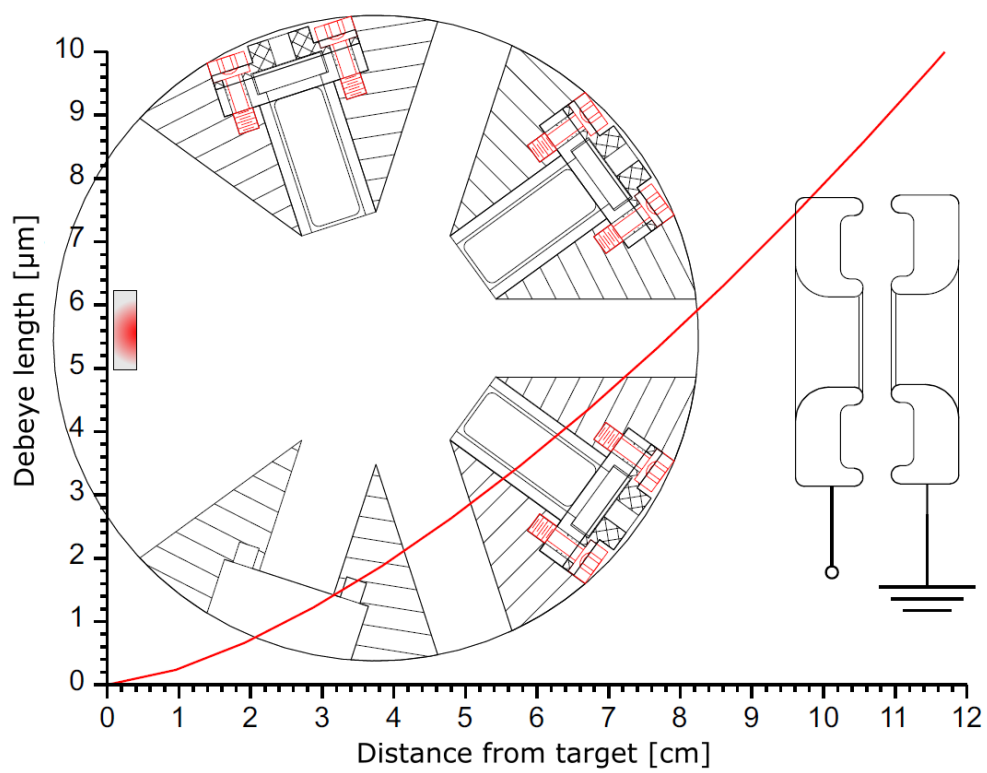
Figure 3.5: Change of the Debye length of the expanding plasma over the distance from the target. The experimental setup is shown in the background. Adapted from [14].

3.2 Beam Line

The complete beam line consists of more different electrostatic components as shown in Figure 3.6 for further experiments, but most of them are not used at the moment and therefore grounded. This is the case with the Einzel lens, quadrupole triplet 1 and all parts of the alternative /extraction beamline. The following discussion focuses on the other parts of the beam line that were used in this experiment.

3.2.1 Quadrupole

The first active part of the beam line is an electrostatic quadrupole deflector. Four electrodes are built in a grounded cuboid shielding. In the plane of the ion path, the shielding is a square. The ions enter on the middle of one side, perpendicular to it, and leave in the same fashion after the bend. The electrodes are orthogonal to the ion path, in the corner of that square. The precise dimensions are unfortunately not known. A voltage U_{qu} is applied to two of them in the opposite corners, $-U_{qu}$ on the others. Inside the square, they produce the potential of a two-dimensional quadrupole field. The desired 90° angle is achieved here if the quadrupole voltage U_{qu} is roughly equivalent to the U_{ex}. A more detailed examination of the voltage needed is done in the next chapter. The advantage of using a quadrupole deflector here is that, for future experiments, it enables the extraction of the ions from the charge breeder into the alternative beam line, if the polarity of the voltage U_{qu} is changed between injection and extraction. This would be much faster than e.g. turning the target wheel as mentioned before. An example of an electrode setup with the resulting equipotentials and ion path can be seen in Figure 3.7, where a quarter of a quadrupole is shown without housing.

3.2.2 Faraday Cup

There are two Faraday cups in the beam line. They both can be moved out of the the beam line and exchanged with apertures of different sizes. For the measurements presented here cup 1 is used and always inside the beam line, but for future experiments, as discussed in Chapter 1, it will be moved out so the ions can enter the charge breeder. If the ions hit the cup their charge is dissipated. There are two ways used here to process that signal:

1. Time-sensitive analysis with an inverting pre-amplifier.

2. Charge-sensitive analysis via indirect measurement of the charge compensation current over a resistance.

In both cases the signal is transduced into a voltage which is measured and saved on a digital storage oscilloscope. It uses the delay gate output as a trigger signal and already takes averages over different shots.

3.2.3   Image-Charge Detector

The image-charge detector designed for this experiment consists of a steel ring with an internal radius of $5\,mm$ and a length of $16\,mm$. To ensure a good signal a shielding was constructed around the ring. A cross section of the ring design can be seen in Figure 3.10. Simulations done in [11] show the spatial dependency of the signal on the ion position as seen in Figure 3.11. It can be seen that ions going through the ring inside a radius of about $3\,mm$ are leading to a peak as they move in z direction. The radial dependency here is very small. Therefore integrating over the number of ions $n(z)$ of charge q and the z response function $f(z)$ gives the charge

$$Q = -q \int_{-\infty}^{\infty} n(z)f(z)\,\mathrm{d}x, \tag{3.1}$$

which can be simplified to

$$Q = -I\sqrt{\frac{m}{2E}} \int_{-\infty}^{\infty} f(z)\,\mathrm{d}x \tag{3.2}$$

as given in [11], depending on the beam current I, the ion mass m and the ion energy E. The integral over $f(z)$ here gives $1.5 \times 10^{-2}\,m$. After the image-charge detector there is another removable Faraday cup, additionally to cup 1, as seen in Figure 3.10, 3.8 and 3.9, between the image-charge detector end the charge breeder. It is split in two circles with different radii to focus the beam. It is also useful to calibrate the image-charge detector. If it is removed, the way in and out of the charge breeder is free, which allows for a bidirectional measurement of the same bunch of ions before and after the charge breeding.
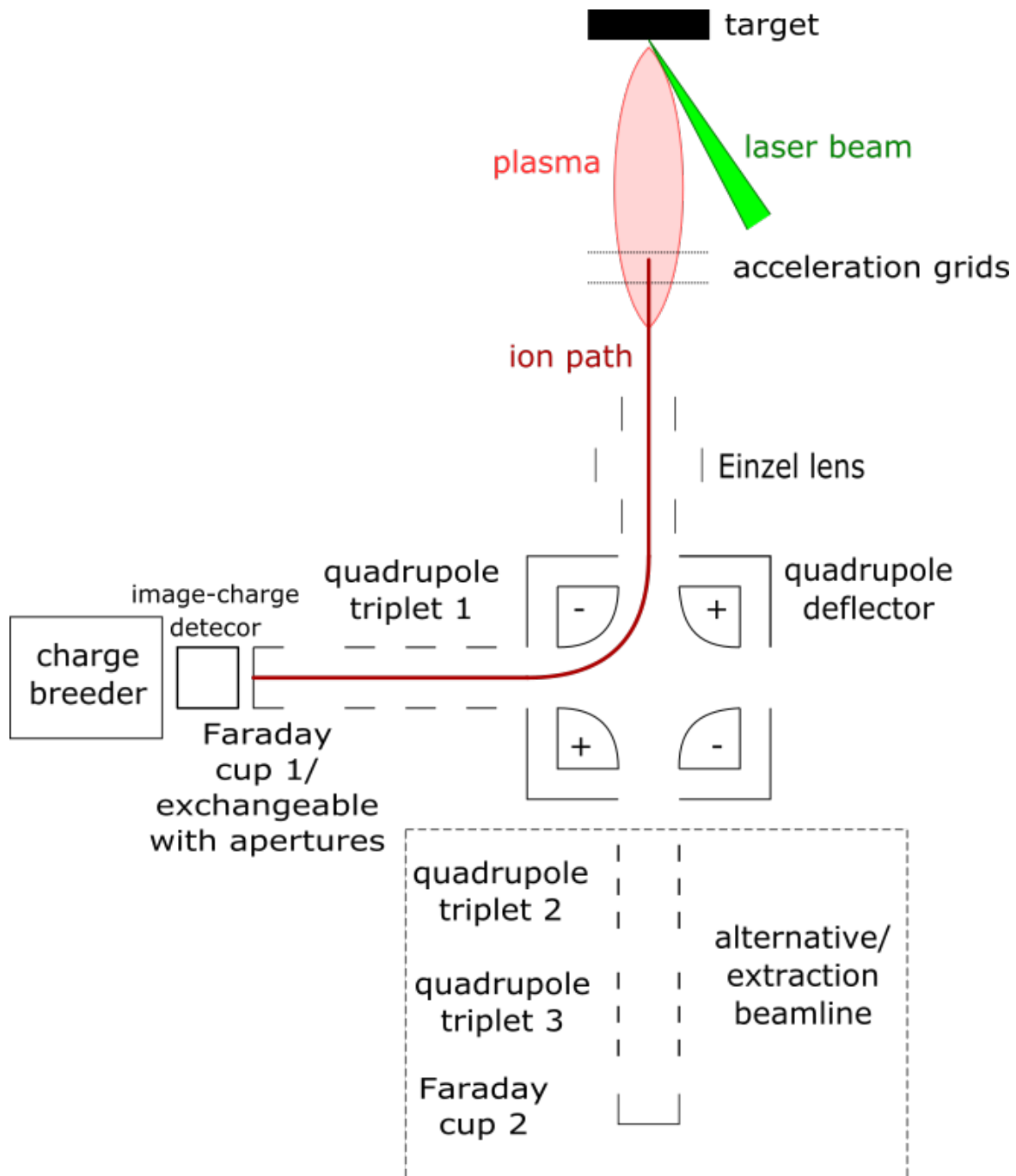
Figure 3.6: Schematic overview of the complete beam line assembly. All elements for the final assembly are shown. The ion path for the experiments conducted here is marked. The charge breeder and the image-charge detector are not yet connected to the beam line. The alternative beam line is connected but not used at the moment. All quadrupole triplets as well as the Einzel lens are grounded for all experiments done in this work.
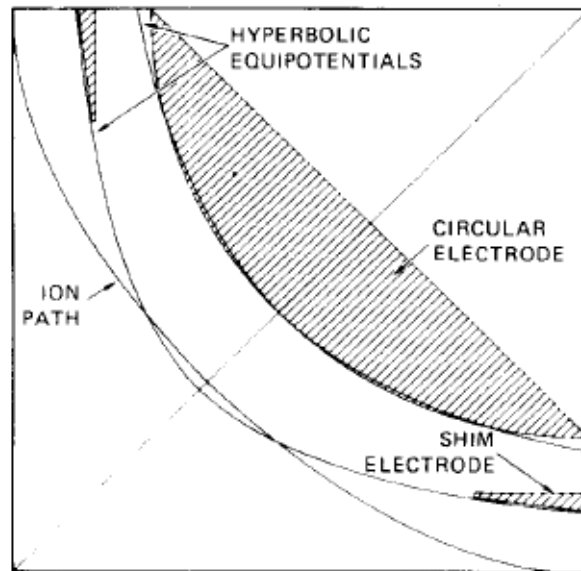
Figure 3.7: Example for the configuration of one of four electrodes to produce a quadrupole field, the equipotentials using all four and the median ion path as found in [16].

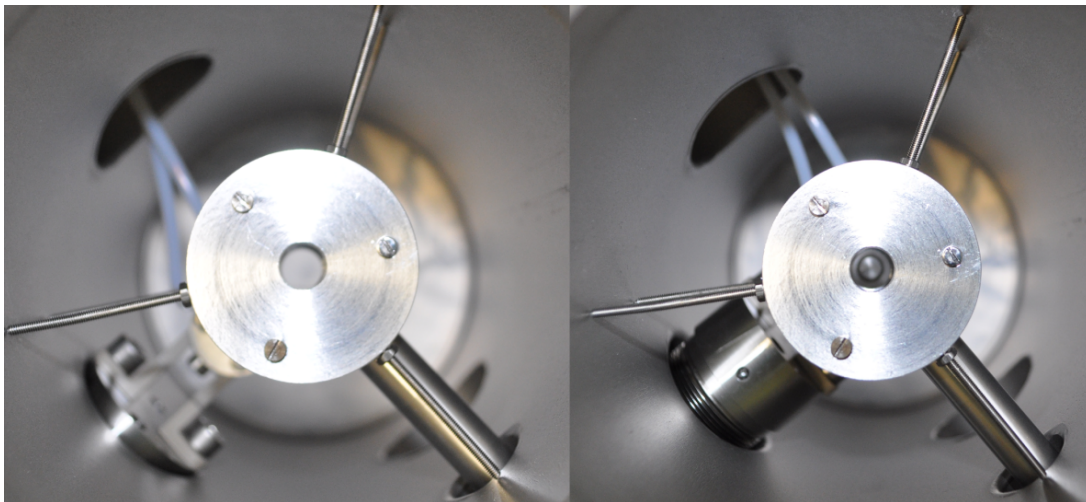Figure 3.8: Photograph of the bidirectional Faraday cup from both sides.

Figure 3.9: Photograph of the image-charge detector in its chamber with (right) and without (left) the removable Faraday cup after the ring.
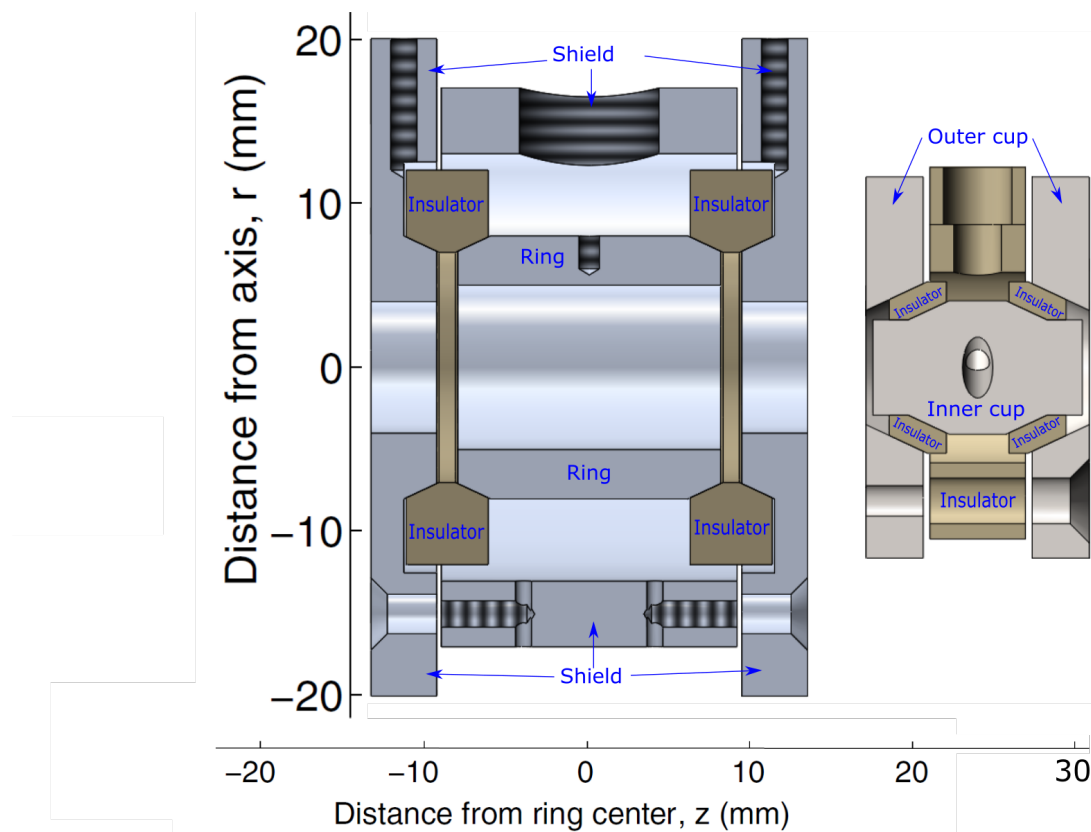
Figure 3.10: Cross-section of the complete new measurement unit. Left: Image-charge detector. The inner ring is separated from the outer shielding via ring insulators. The shielding is grounded and leads to a coaxial signaling path. Right: Bidirectional Faraday cup. The inner and outer targets are separated from each other via insulators but connected to both sides of the cup. They are connected to a manipulator via an insulator which allows to remove the cup while it is not needed. The distance between cup and image-charge detector may vary in the later assembly, the rest is on scale.
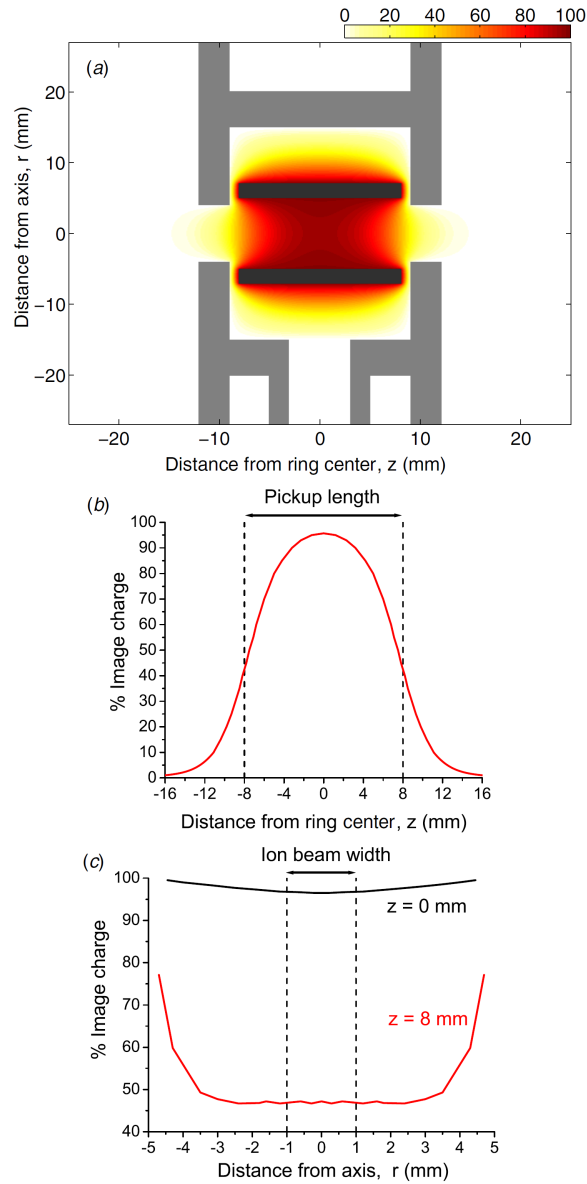
Figure 3.11: (a) Two-dimensional variation in the percentage image charge response. Function of r and z. (b) Fraction of image-charge response at the pickup axis $r = 0 \, \text{mm}$ as function of z (c) Fraction of image-charge response at the pickup centre $z = 0 \, \text{mm}$ and pickup edge $z = 8 \, \text{mm}$ as function of r. From [11].

Chapter 4

Measurements

All following experiments were done on the the Faraday cup 1 as explained in Chapter 3.2.2

4.1 General Types of Analysis

The signal of a single shot to the next varies quite a bit and contains a lot of background noise. To get rid of most of those effects directly, the oscilloscope is programmed to take averages over a certain number of shots. The number of averages taken depends on the purpose of the spectrum, since there are different problems with a lot of averages for every measurement:

1. The delay gate doesn't work correctly and sometimes increases the delay time for a couple of shots. If the averages are taken over too many shots, the delay time therefore is not constant. If that happened or not can be checked by comparing the average delay time with the delay time of single shots to sort out such spectra.

2. Each shot increases the crater on the target surface. After too many shots, the laser needs to be refocused or the target must be moved slightly to keep a similar power density.

3. Since the repetition rate of the laser is fixed, too many averages just take too much time for the measurements.

It has to be noted that especially for the charge-sensitive measurements as explained in 3.2.2 problem 1 and 2 are quite relevant since they have a direct effect on the charge extracted. So less averages are used for them than for the time of flight, which does directly depend on these effects.

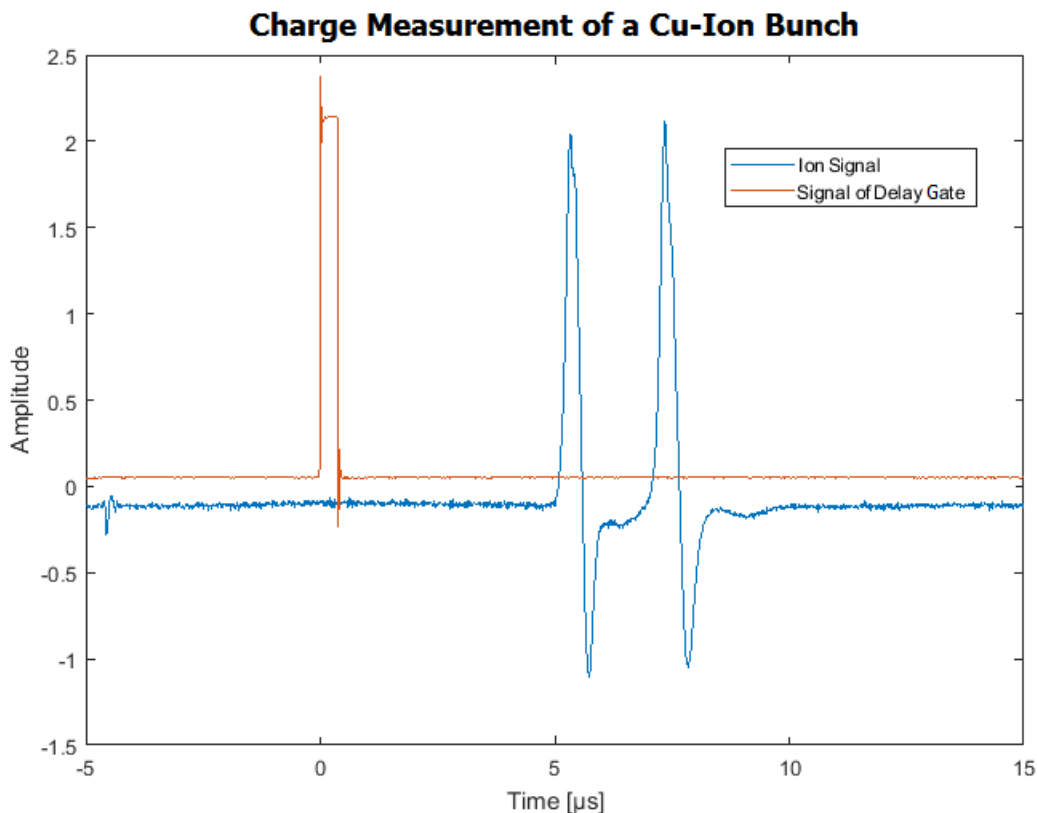## 4.2 Charge Measurement for Different Parameters

Figure 4.1: Charge-sensitive measurement of ions using a resistor. Shown is the voltage over the resistor as measured on the oscilloscope as well as signal steering the high voltage from the delay gate, marking the start time of ion acceleration, over time.

For this measurements the Faraday cup was connected to the oscilloscope and a resistor in parallel. The obtained data is visualized in Figure 4.1. With the internal resistance of the oscilloscope of $1\,\mathrm{M\Omega}$ and of the resistor of $501.8(5)\,\Omega$, this leads to an total resistance of $501.5(5)\,\Omega$. This allows to calculate the charge of a bunch of ions using

$$Q = \int I\,\mathrm{d}t = \int \frac{U}{R}\,\mathrm{d}t = \frac{1}{R}\int U\,\mathrm{d}t. \tag{4.1}$$

where I is the current over the resistor, U the voltage and t the time measured with the oscilloscope. This allows us to integrate $\int U\mathrm{d}t$ numerically. This was done using a trapezoidal

method after the background was subtracted using a polynomial fit. For the endpoints of the integration interval the time where the voltage reaches nearly zero was used. The negative peaks are from the current recharging the capacity in the cup rather than from incoming ions and are therefore not included. Since this process starts before that moment there is a systematical error introduced. Therefore it has an influence on the total charge measured, but not on the optimal parameters, since the effect is proportional to the measured charge.

4.2.1   Uncertainty Estimation

To estimate the uncertainty of the charge values, twelve measurements were done with the same parameters. There are small changes in the delay time but that influence was left in, since this increases the uncertainty and might have occurred in some shots of the following measurements as well, even if measurements with clear differences were excluded. The values for ions with $q = 1+$ and $q = 2+$ were considered separately to get the uncertainty of the measurement of individual charge states as well as added up, both in ion number and in total charge, to get the uncertainty on combined evaluation. Combined evaluation was done when the analyzed parameter didn't influence the ratio of the different charge states. The extra evaluation is necessary as they are not independent with from each other with an unknown correlation and a propagation of uncertainties might lead to an overestimated uncertainty, as the correlation may be negative. The uncertainties found are

$$\frac{\Delta n_{1+}}{n_{1+}} = \frac{\Delta q_{2+}}{q_{2+}} = 14.7\,\%$$

$$\frac{\Delta n_{2+}}{n_{2+}} = \frac{\Delta q_{2+}}{q_{2+}} = 8.2\,\%$$

$$\frac{\Delta(n_{1+} + n_{2+})}{(n_{1+} + n_{2+})} = 8.6\,\%$$

$$\frac{\Delta(q_{1+} + q_{2+})}{(q_{1+} + q_{2+})} = 5.4\,\%$$

for measurements averaging over 16 shots. The correlation seems to be negative, is justified if one assumes that more singly charged ion lead to less doubly charged ions and vice versa, e.g. because a certain ionization energy provided to a system can either lead to more singly charged ions or ionize them to doubly charged ions. This shows that for the combined evaluation adding up the total charge of ions leads to better results than adding up their number.
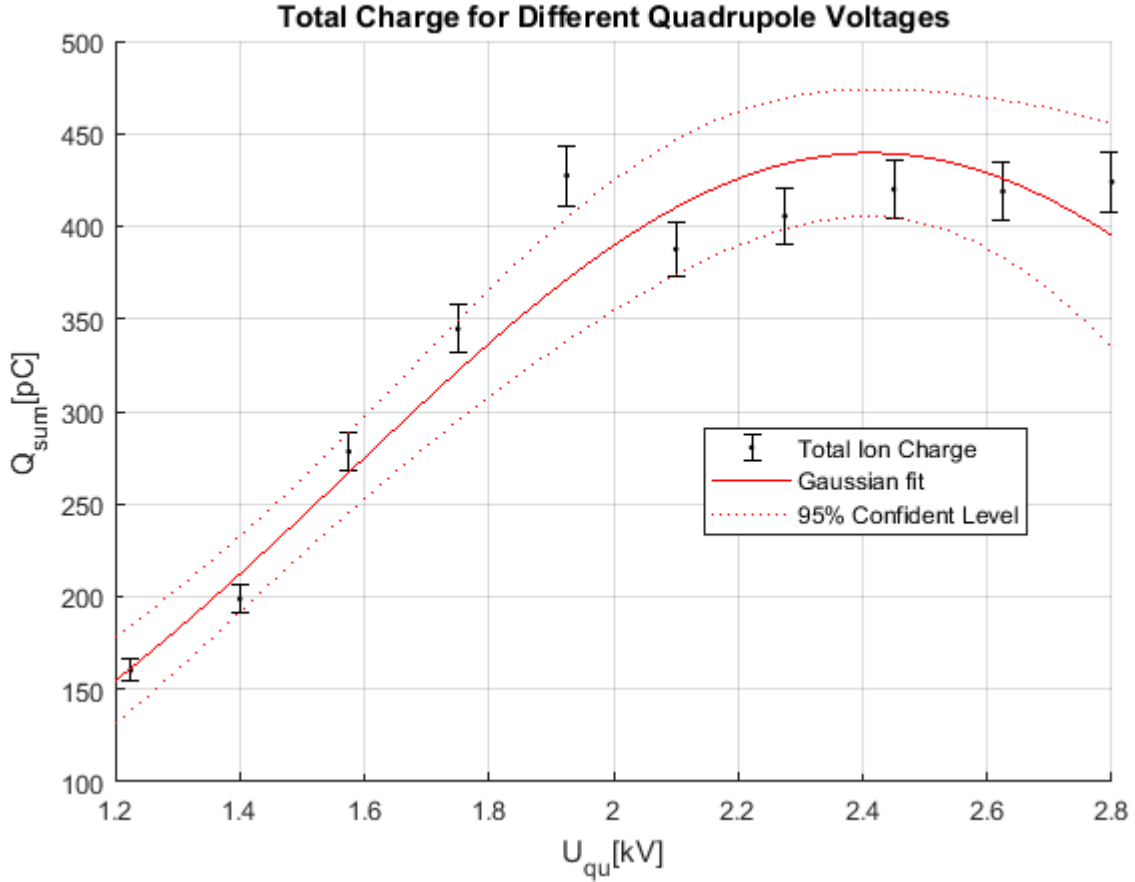
4.2.2   Quadrupole Voltage

Figure 4.2: Measurement of the total ion charge per shot for different quadrupole voltages U_{qu} for an extraction voltage $U_{ex} = 2.4507(18)\,\text{kV}$. A Gaussian distribution was fitted on the measured data.

Since we neither know the energy of the ion beam, only that the extraction voltage can assumed to be proportional to it, nor the exact geometry of the quadrupole bender, we do not know which voltages lead to the optimal path through the quadrupole. Therefore a measurement with changing quadrupole voltages was conducted to find out where the most charge hits the cup. A copper target was used. The fixed parameters were

- extraction voltage $U_{ex} = 2.4507(18)\,\text{kV}$

- delay time $t_d = 4.50(5)\,\text{µs}$

- pulse length $t_{\mathrm{p}} = 130(2)\,\mathrm{ns}$

- Number of shots averaged per measurement $= 8$.

The path through the bender does not depend on the charge state, therefore the total charge was added up. The uncertainties of the times are included in the $5.4\,\%$ as stated above, so no further consideration is needed for them. The uncertainty of U_{ex} is used for the calculation of the uncertainty of the voltage ratio. The measurement was done twice for every value of U_{qu}, first going down with its voltage and then going up again. Since there is an increasing difference between two measurements at the same voltages the more shots lie in between, there is a falling drift over the measurements. Assuming that the trend can be approximated linearly, this is compensated by adding up the two measurements for each quadrupole voltage, since this gives the sum of the first and last measurement, the second and the next to last etc. This leads to a contribution of $16 + 16 = 32$ shots per measured value for both charge states, therefore the uncertainty on each value is $\frac{5.4\,\%}{\sqrt{2}} = 3.8\,\%$. It is assumed that the dispersion of the beam can be approximated with a Gaussian. Therefore a Gaussian is fitted on the resulting values, as it can be seen in Figure 4.2. The resulting best quadrupole voltage is $U_{\mathrm{qu}} = 2.41(18)\,\mathrm{kV}$, which leads to a ratio

$$\frac{U_{\mathrm{qu}}}{U_{\mathrm{ex}}} = 0.983(73). \tag{4.2}$$

4.2.3 Delay Time

The influence of the delay time t_{d} on the charge was analyzed next. Since this is the time between the laser shot and the charge separation between the grids it equals a selection of a slice of plasma propagating through the vacuum chamber. This leads on the one hand to a Maxwell-Boltzmann distribution [14] and on the other hand to different charge distributions for different delay times because the plasma temperature is not constant in the plasma as discussed in Chapter 2. Therefore the plasma "selected" with small t_{d} is colder, leading to a higher fraction of $q = 1+$, than plasma with higher t_{d}, where the amount of $q = 2+$ ions increases. Hence the individual charge states, with their subsequent uncertainties, are used for the following fits of Maxwell-Boltzmann distributions done in Figure 4.3 and 4.4. The maximum charge was received at

$$t_{\mathrm{d}} = 4.42(56)\,\mathrm{\mu s} \text{ for } q = 1+ \tag{4.3}$$

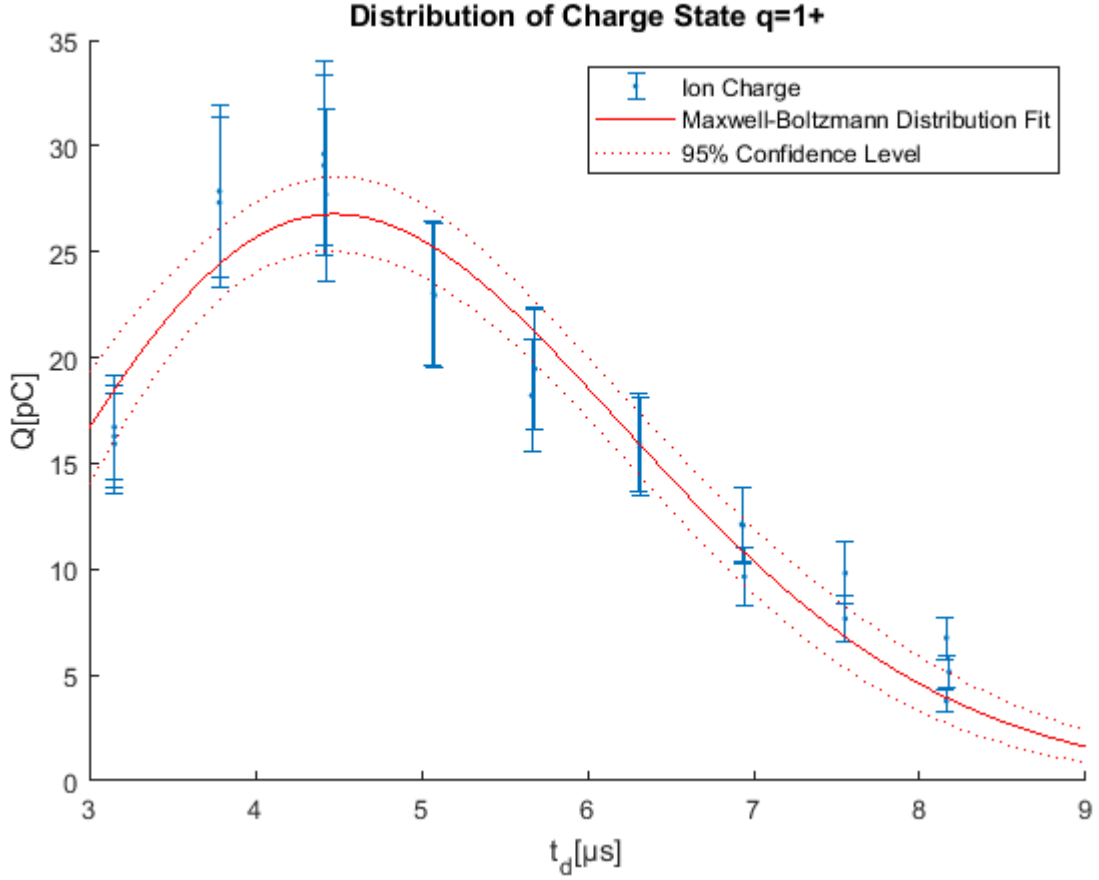$$t_{\mathrm{d}} = 6.3(14)\,\mathrm{\mu s} \text{ for } q = 2+ \tag{4.4}$$

Figure 4.3: Charge of all singly charged ions at different delay times t_{d}. A Maxwell-Boltzman distribution was fitted.

respectively. This leads to an estimation of the drift energy of

$$E_0 = 83(21)\,\mathrm{eV} \text{ for } q = 1+ \tag{4.5}$$

$$E_0 = 41(18)\,\mathrm{eV} \text{ for } q = 2+ \tag{4.6}$$

4.2.4   Pulse Length

If we increase the pulse length t_{p} more charge separations take place between the two grids and therefore more ions are accelerated. Since the pulse lengths, with $75\,\mathrm{ns} < t_{\mathrm{p}} < 453\,\mathrm{ns}$, are well below the length of the time delay, here at $4.42(10)\,\mu\mathrm{s}$, the change in plasma temperature doesn't
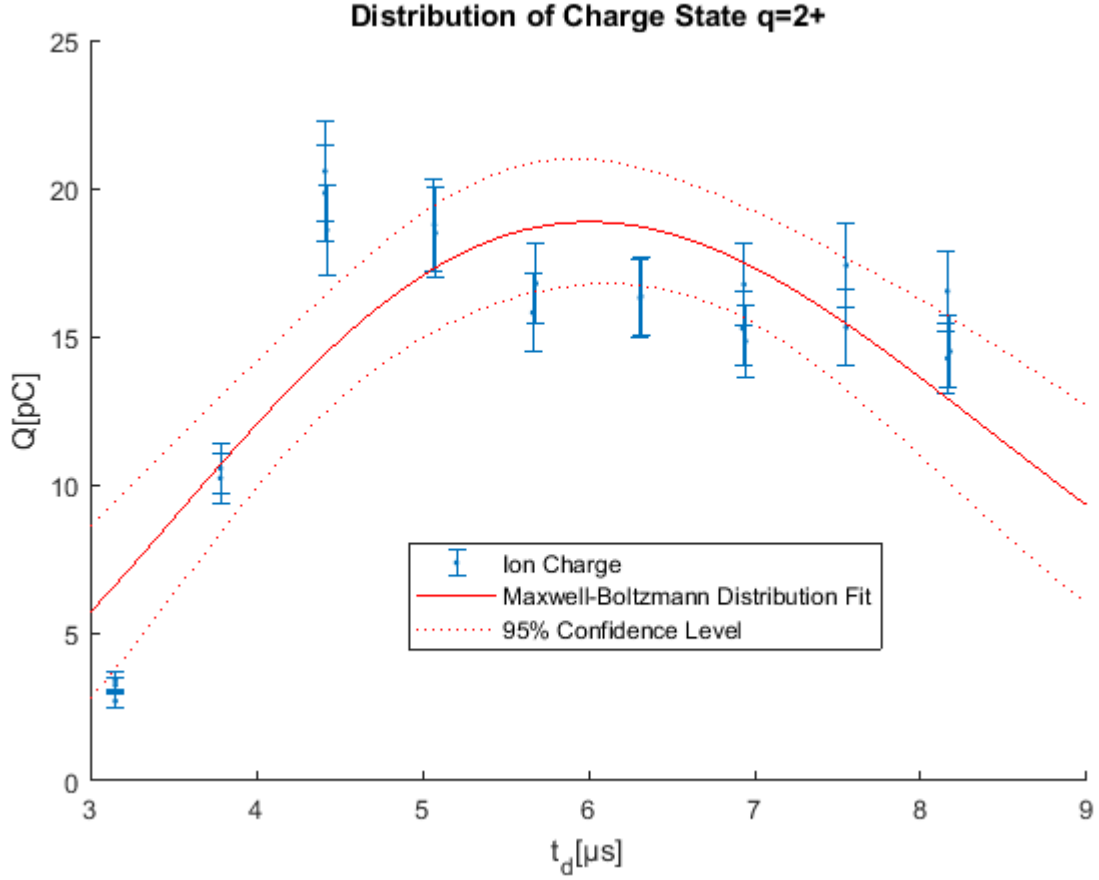
Figure 4.4: Charge of doubly charged ions at different delay times t_{d}. A Maxwell-Boltzman distribution was fitted.

have a strong impact, so the ratio $\frac{n_{1+}}{n_{2+}}$ is assumed to be roughly the same. For this short pulse lengths there is a roughly linear increase in charge with t_{p}, as can be seen in Figure 4.5. For longer pulse lengths, there is a saturation expected after the whole plasma between the grids was accelerated. Because of the charge separation occurring before the first grid as well, no new plasma enters that part of the experimental setup while the voltage is applied. An increase in t_{p} also leads to a broadening of the signal in time domain.
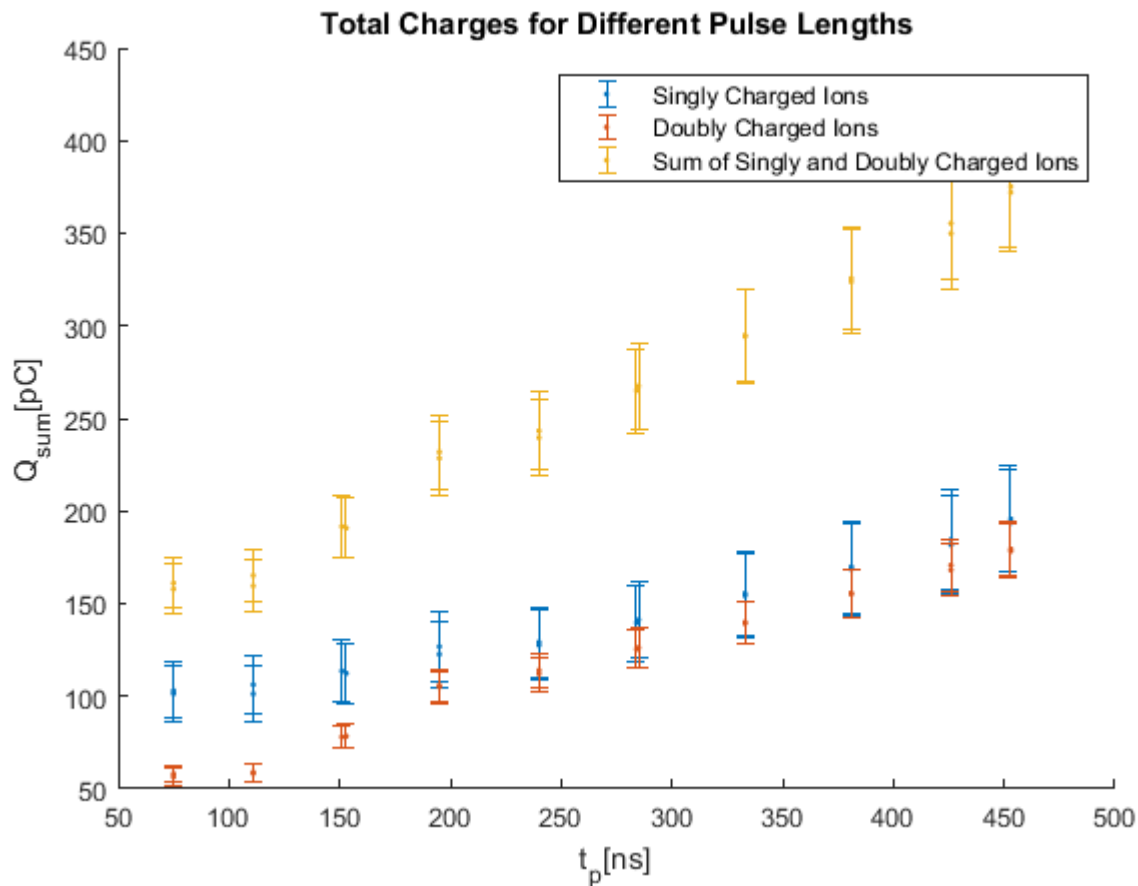
Figure 4.5: Charge measured for increasing pulse length t_{p}.

4.3   Time of Flight Measurements

For a better time resolution in the Time of Flight (TOF) measurements, the resistor was removed and an inverting pre-amplifier was used instead. As can be seen in Figure 4.6 this can lead to positive peaks before and after the negative signal peak itself which make the exact absolute location of the peak unclear, but enables one to make more precise relative measurements that even allows to distinguish ions from the two different copper isotopes Cu-63 and Cu-65. The uncertainty of the absolute peak location is in the region of the uncertainty due to the length of the HV signal and is therefore neglected for this measurements.
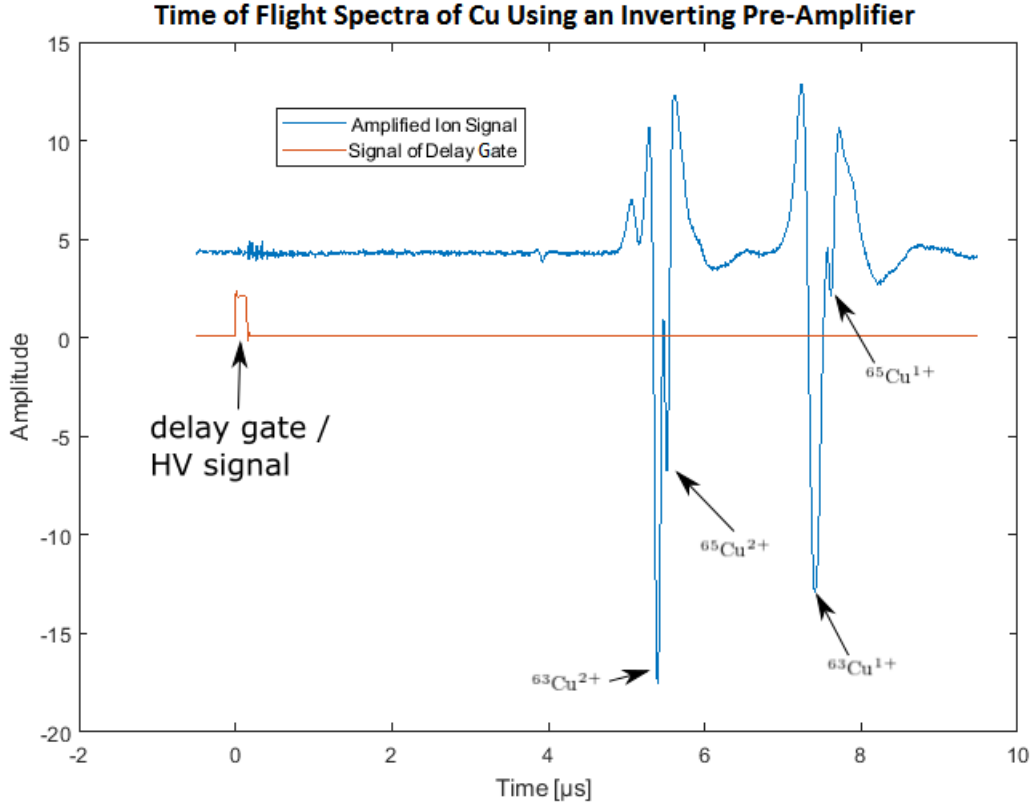
Figure 4.6: Example of a time of flight measurement using a copper target. The peaks could be identified as different isotopes and charge states of copper. The small peak at 4 µs might be from $q = 3$ ions, although the position is a bit off if we assume the big peak to be the position of the other charge states.

4.3.1 Contributions to the TOF Values

There are several contributions to the measured time of flight:

- Time difference between the point in time the delay gate output signal that triggers the oscilloscope and the point where the high voltage at the output of the switch is built up. According to [18] the switch has a typical rise time of 25 ns. The difference in signal travel time with a difference of cable length of under a meter is under 3.3 ns. This therefore contributes a small systematical error on the starting time t_{sys}.

- The flight time while the charge separation and acceleration takes place. That time obvi-

ously is below the pulse length $t_\mathrm{p} = 163(2)\,\mathrm{ns}$. The contributed distance

$$s_\mathrm{acc} = \frac{1}{2} U_\mathrm{acc} \frac{q}{m} t_\mathrm{acc}^2 + t_\mathrm{acc} \sqrt{2 \frac{E_0}{m}} \qquad (4.7)$$

hereby has to be below the difference of the grid position of $5\,\mathrm{mm}$ and of the same magnitude as the Debye length of $8.5\,\mathrm{\mu m}$, as discussed in Chapter 2.

- The flight in the free space without an outer electrical field. The distance

$$s_\mathrm{free} = t_\mathrm{free} \sqrt{2 \frac{U_\mathrm{acc} q + E_0}{m}} \qquad (4.8)$$

  covered here is the largest contribution.

- The time inside the conservative accelerating field of the quadrupole, which results in a distance

$$s_\mathrm{qu} = t_\mathrm{qu} \sqrt{2 \frac{U_\mathrm{acc} q + E_0}{m}} + a_\tau t_\mathrm{qu}^2 \qquad (4.9)$$

  depending on the unknown time and acceleration inside the quadrupole.

Summing up these contributions leads to the total distance

$$s_\Sigma = a_\tau t_\mathrm{qu}^2 + (t_\Sigma - t_\mathrm{acc} - t_\mathrm{sys}) \sqrt{2 \frac{U_\mathrm{acc} q + E_0}{m}} + 0.5 U_\mathrm{acc} \frac{q}{m} t_\mathrm{acc}^2 + t_\mathrm{acc} \sqrt{2 \frac{E_0}{m}} \qquad (4.10)$$

Now, some approximations are done to exclude some of the unknown contribution to that equation. First of all $s_\mathrm{acc} \ll s_\Sigma$, therefore all of the acceleration terms are dropped for the calculation an included in the uncertainty estimation instead. In the consequential calculated time of flight

$$t_\Sigma = \sqrt{\frac{m}{2(U_\mathrm{acc} q + E_0)}} \left(s_\Sigma - a_\tau t_\mathrm{qu}^2 \right) + t_\mathrm{sys} \qquad (4.11)$$

we approximate $E_0 \ll U_\mathrm{acc} q$ and therefore move that part to the uncertainty estimation as well, leading to

$$t_\Sigma = \sqrt{\frac{m}{2 U_\mathrm{acc} q}} \left(s_\Sigma - a_\tau t_\mathrm{qu}^2 \right) + t_\mathrm{sys}, \qquad (4.12)$$

where we replace the unknown quadrupole parameters a_τ as discussed in Chapter 2, to

$$a_\tau = A \frac{q U_\mathrm{qu}}{m}. \qquad (4.13)$$

This leads to

$$t_\Sigma = \sqrt{\frac{m}{2U_{\mathrm{acc}}q}} \left(s_\Sigma - A\frac{qU_{\mathrm{qut}_{\mathrm{qu}}^2}}{m}\right) + t_{\mathrm{sys}}, \tag{4.14}$$

unfortunately the unknown path-length through the quadrupole prevents us from further estimation of t_{qu}^2 using Equation 4.9.

4.3.2 Energy of the Ions

Measurements with different extraction voltages U_{ex} and quadrupole voltages U_{qu} were done for a copper target. That enables one to estimate the proportionality k between applied acceleration voltage and resulting acceleration voltage:

$$U_{\mathrm{acc}} = kU_{\mathrm{ex}}$$

Unfortunately the A introduced in Equation 4.13 can not be properly estimated, but is approximated by a constant t_{qu} to compensate for at least some of the effects. This is done in two separate fits for the different charge states $q1+, q2+$. We get:

$$k = 0.918(50) \text{ for } q = 1+ \tag{4.15}$$

$$k = 0.957(31) \text{ for } q = 2+ \tag{4.16}$$

4.3.3 Relative Mass Measurement

Now different targets are used to figure out whether an analysis of the target properties is possible. The targets used here are made out of aluminum, copper and molybdenum. The received signals can be seen in Figures 4.7, 4.8 and 4.9. Here the different isotopic properties of the targets are visible: Aluminum, consisting only of the isotope Al-27, shows one clear peak for every charge state. Copper, consisting of Cu-63 and Cu-65, has two distinguishable peaks. Molybdenum, consisting of seven different isotopes between Mo-92 and Mo-100, shows a broadened signal with different peaks visible but not fully distinguishable. Since the copper peaks are on the edge of being distinct, one can make a rough estimation of the resolution R of the measurement setup:

$$R = \frac{m}{\Delta m} \geq \frac{65\,\mathrm{u}}{65\,\mathrm{u} - 63\,\mathrm{u}} = 32.5 \tag{4.17}$$
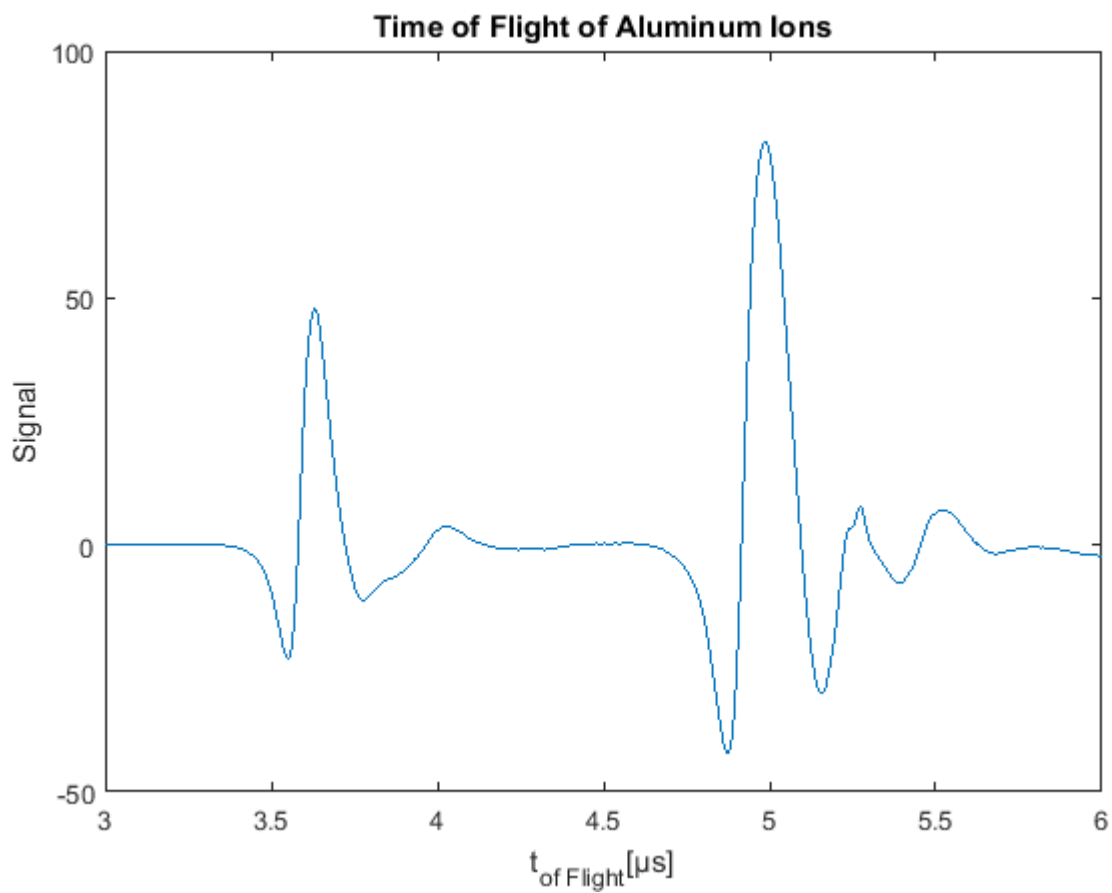
Figure 4.7: TOF spectrum of aluminum. As aluminum only has one isotope, clear peaks for singly and doubly charged ions are visible.
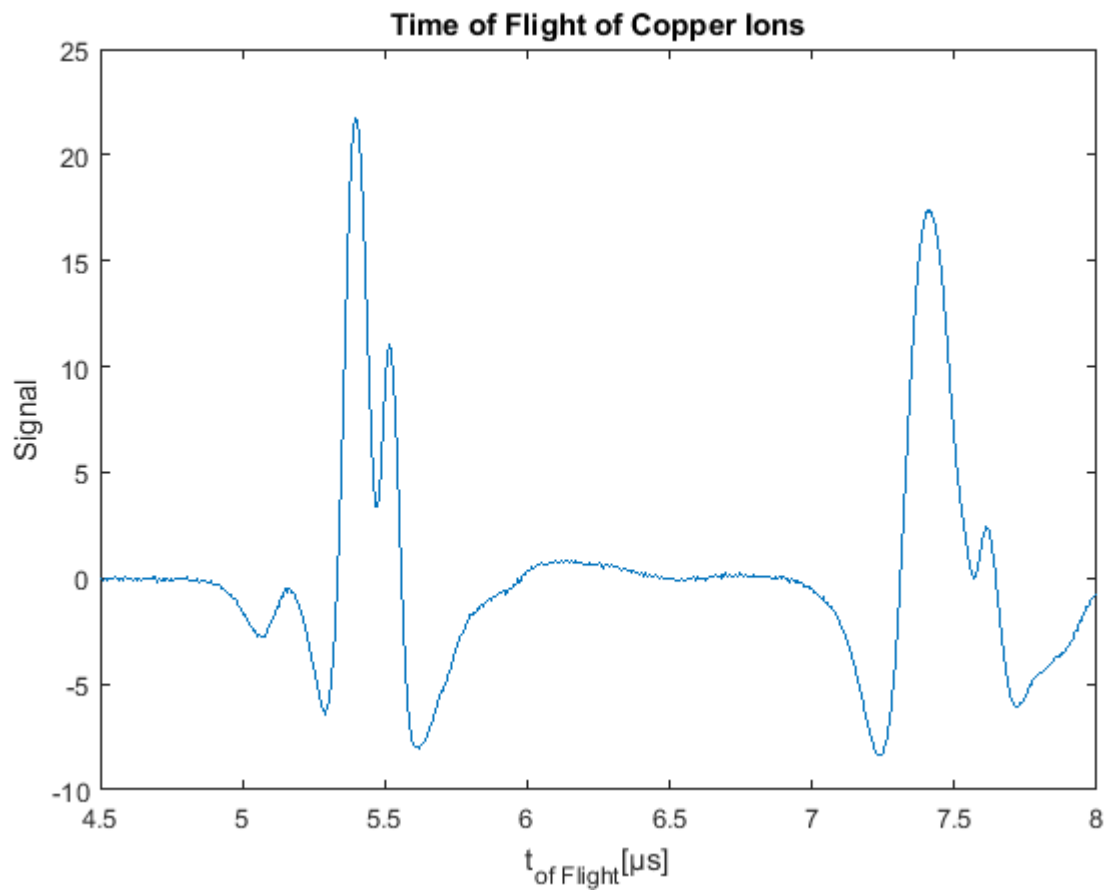
Figure 4.8: TOF spectrum of copper. Both isotopes are visible for singly and doubly charged ions.
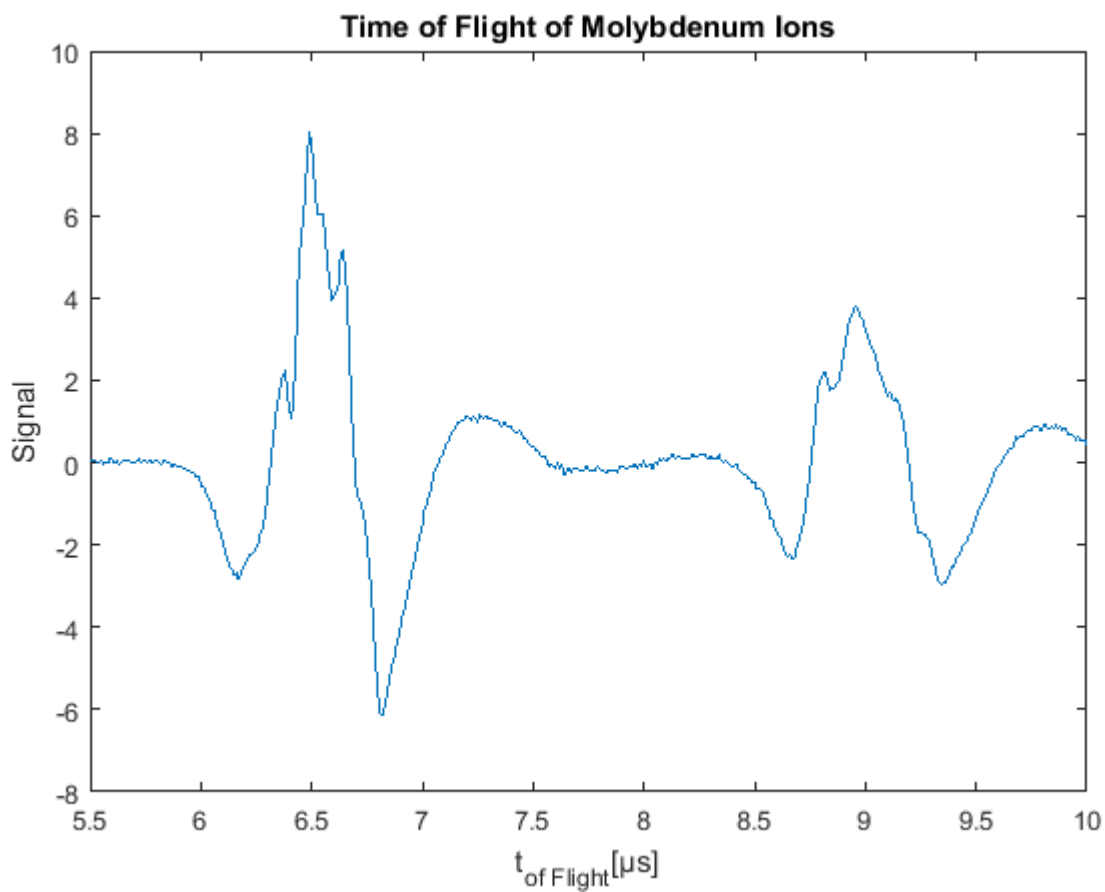
Figure 4.9: TOF spectrum of molybdenum. Since it has seven naturally occurring isotopes the peaks for both charge states are quite broad and rough. Since they are closer together than for copper and of different abundances, they are not distinguishable.

Chapter 5

Conclusion and Outlook

The LIONS is capable of producing ions in the charge states $q = 1+$ and $q = 2+$. At a voltage ratio of $\frac{U_{\text{qu}}}{U_{\text{ex}}} = 0.983(73)$ the beam has the ideal way through the quadrupole. The maximum number of singly charged ions is reached at a delay time of $t_{\text{d}} = 4.42(56)\,\mu\text{s}$ for $q = 1+$. With a pulse time of $t_{\text{p}} = 453(1)\,\text{ns}$—which was the longest pulse time used for the measurements—one pulse of singly charged ions has a total charge of $Q_{\text{pulse}} = 183(27)\,\text{pC}$ which corresponds to $N_{\text{q1+}} = 1.14(17) \times 10^9$ ions. That number should be sufficient to make tests of the charge breeder, as it is well above the 3×10^9 needed for the image-charge detector, even for a low efficiency. The energy of the injected ions was roughly estimated as qkU_{ex} with $k = 0.918(50)$ for $q = 1+$ and $k = 0.957(31)$ for $q = 2+$. The estimation could be improved a lot if the dimensions of the beam line setup would be known more precisely. The resolution of the mass measurement with the Faraday cup and the pre-amplifier was estimated as $R = m/\Delta m \geq 32.5$. This could be improved even more with increasing the distance between target and cup, probably at the expense of ion number. Therefore it was not done here, as the goal was to identify the charge distribution, which is clearly possible there, at high ion numbers. A drawback of the current setup is that there is no possibility to filter the ions according to their charge state which leads to an injection of doubly charged ions into the charge breeder as well, which makes the efficiency measurement more difficult. Choosing an even lower delay time than the one mentioned above increases the $N_{\text{q1+}}/N_{\text{q2+}}$ ratio at the cost of total ion number.

The next step is to test the image-charge detector and calibrate it using the new cup. Then the charge distribution injected is going to be measured and compared with the charge extracted after breeding. One also has to check if the image-charge detector can be calibrated time sensitive enough to measure a charge distribution directly. If that is not the case, one could use it in combination with the new cup to measure the charge distribution of injected ions, basically

a roughly constant ratio between N_{q1+}/N_{q2+}. This allows ont to get the charge distribution of injected ions out of a total charge measurement on the image-charge detector. The charge distribution of the extracted ions then can be measured on the Faraday cup on the alternative beam line. Here the non-charge selective property of the quadrupole bender might prove to be useful. This way, injection and extraction charge distributions can be compared with this setup, even if the image-charge detector designed here might not prove to be time sensitive enough. This allows us to test if the EBIT fulfills all desired properties for the use as a charge breeder. The EBIT will be used later to charge-breed bunches of singly charged, rare isotopes enough so they have a mass-to-charge ratio between $5\,\mathrm{u}\,e^{-1}$ and $7\,\mathrm{u}\,e^{-1}$. Since the isotopes have very short life times it is essential that this happens quite fast. The injection with ions from the LIONS and later measurement of the extraction allows to optimize the EBIT for that task and to check if it fulfills all needed properties.

Bibliography

[1] W. von Heisenberg, *Physics and Philosophy: The Revolution in Modern Science.* 1958.

[2] T. Kirchoff and N. C. Karafyllis, *Naturphilosophie.* 2017.

[3] L. G. Marciano, *Die Vorsokratiker 3.*

[4] J. Dalton, *A New System of Chemical Philosophy.* 1808.

[5] W. Kuhn, *Ideengeschichte der Physik.* 2016.

[6] D. B. Herrmann, *Urknall im Labor: Wie Teilchenbeschleuniger die Natur simulieren.* 2010.

[7] R. Locqueneux, *Kurze Geschichte der Physik.* 1989.

[8] J. H. Hamilton, S. Hofmann, and Y. T. Oganessian, "Search for superheavy nuclei," 2013.

[9] J. Dilling, R. Krücken, and L. Merminga, "Ariel overview," 2013.

[10] M. Marchetto, R. A. Baartman, and R. E. Laxdal, "Ariel front end," 2013.

[11] J. Alexander, L. Graham, C. R. Calvert, O. Kelly, R. B. King, I. D. Williams, and J. B. Greenwood, "Determination of absolute ion yields from a maldi source through calibration of an image-charge detector," 2010.

[12] M. Eichhorn, *Laserphysik.* 2013.

[13] B. Wolf, *Handbook of Ion Sources.* 1995.

[14] A. A. Werdich, "Konstruktion und Aufbau einer Laser-Ionenquelle für die Freiburger Elektronenstrahl-Ionenfalle," 2000.

[15] M. von Allmen and A. Blatter, *Laser-Beam Interactions with Materials.* 1995.

[16] H. D. Zeman, "Deflection of an ion beam in the two-dimensional electrostatic quadrupole field," 1977.

[17] L. Schmöger, "Ein elektrodynamisches System für den Transfer hochgeladener Ionen in eine Paulfalle," 2013.

[18] Behlke Power Electronics GmbH, "High voltage push pull switching units," -.

Erklärung

Ich versichere, dass ich diese Arbeit selbstständig verfasst und keine anderen als die angegebenen Quellen und Hilfsmittel benutzt habe.

Heidelberg, den 31. 07. 2017,